This is a preprint of a published paper in "Engineering Fracture Mechanics" by Elsevier availabe at https://doi.org/10.1016/j.engfracmech.2017.08.021

A novel development of bi-level reduced surrogate model to predict ductile fracture behaviors

Yuliang Hou[a,b,*], Thaneshan Sapanathan[b,c], Alexandre Dumon[d], Pierre Culière[d], Mohamed Rachik[b]

[a]*School of Mechanical Engineering, Zhengzhou University, Science Road 100, 450001, Zhengzhou,China*
[b]*Laboratoire Roberval, CNRS UMR7337, Sorbonne université, Université de Technologie de Compiègne, Centre de recherche Royallieu, CS60319, 60203, Compiègne Cedex, France*
[c]*Institute of Mechanics, Materials and Civil Engineering, Université catholique de Louvain, B-1348 Louvain-la-Neuve, Belgium*
[d]*ESI Group, 99 Rue des Solets, BP80112, 94513, Rungis Cedex, France*

Abstract

In this paper, a bi-level reduced surrogate model is developed and presented to identify the material parameters of ductile fracture criterion. Using this method, the identification process becomes feasible with only a limited number of experimental tests. The method assembles local critical elements associated with global models. The surrogate model of fracture strain constructed using Diffuse Approximation and the local elements, reduces the computational effort for searching identified material parameters. Global fracture simulations are preformed to update the target fracture strain and to compute the corresponding failure onset displacement. Convincing results are obtained via *successive* applications of Design of Experiments (DOE) and *enhanced* design space transformation algorithms. The proposed identification protocol is validated for the modified Mohr-Coulomb fracture criterion using DP590 steel. Robustness of this method is confirmed with different initial guess. It orients a new direction for material parameters identification based on surrogate model which can effectively be implemented to predict the fracture behavior.

Keywords: Ductile fracture, Modified Mohr-Coulomb, Surrogate model, Diffuse Approximation, Successive DOE

1. Introduction

Light weight materials become attractive alternatives for modern engineering applications, particularly in the automotive industry, to reduce the emission of environmental pollutants and increase the fuel efficiency. Hence, dual-phase (DP) steel is a promising candidate for this purpose. Commonly, DP steel consists of hard martensite islands embedded into soft ferrite matrix, thereby it enhances several mechanical properties, such as, relatively high ultimate tensile strength (UTS),

*Corresponding author.
Email address: yulianghou@zzu.edu.cn (Yuliang Hou)

Nomenclature

A_0	initial cross section aera of tensile specimen
A_f	fractured cross section aera of tensile specimen
c_1	coefficient of friction
c_2	shear resistance
c_3, c_4, c_θ	material constants of MMC fracture criterion
$D(\bar{\varepsilon}_p)$	damage indicator
d_f	predicted fracture onset displacement
d_f^{exp}	measured fracture onset displacement
Δd_f	adaptive deviation of fracture onset displacement
K	material constant of Swift power law
n	material constant of Swift power law
R	notch radius of tensile specimen
ε_0	material constant of Swift power law
ε_f	initial fracture strain
$\bar{\varepsilon}_f$	equivalent plastic strain to fracture
$\tilde{\varepsilon}_f$	predicted fracture strain
ε_f^{exp}	measured fracture strain
ε_p	plastic strain
η	stress triaxiality
$\boldsymbol{\sigma}$	stress tensor
σ	true stress
$\bar{\sigma}$	von Mises equivalent stress
σ_{I-III}	principal stresses
σ_m	hydrostatic stress
σ_n	normal stress
τ	shear stress
θ	Lode angle parameter
$\bar{\theta}$	normalized Lode angle parameter
$LES.$	least square error
UTS	ultimate tensile strength

low yield to tensile strength ratio, absence of yield elongation [1–6]. However, the application of DP steel in the automotive industry is usually limited by its ductile fracture behavior during forming processes [7–10].

In general, ductile damage occurs as a result of nucleation, growth and coalescence of micro voids that eventually leads to ductile fracture due to crack formation and its propagation [11–15]. In theory, the assumption that the void volume fraction reaches a critical value has been considered as the fundamental hypothesis to explain the ductile fracture criterion. Alternatively, phenomenological models have been proposed to predict ductile fracture without modeling micro-voids. The developments of these models are based on a reasonable assumption that the ductile failure appears when a weighting indicator of the accumulated plastic strain reaches a critical threshold value [16, 17]. According to Bao and Wierzbicki [18], all these models cannot provide an accurate prediction of fracture behavior for a given material within a large range of stress triaxialities. Therefore, Bai and Wierzbicki [19, 20] extended the classical Mohr-Coulomb fracture criterion [21] to predict ductile fracture, which is also called as modified Mohr-Coulomb (MMC) criterion. The weighting indicator of MMC criterion includes the equivalent plastic strain, stress triaxiality and Lode angle parameter.

Recently, numerous experimental investigations [18, 22–28] have been performed to characterize and identify the material parameters which are prerequisite of MMC criterion for various ductile metals. Typically, a massive quantity of fracture tests are required to be performed during such experimental works. This requires enormous amount of time and expenses to prepare specimens and analyze experimental data. Therefore, it indicates the needs for further improvement in this technique to simplify the identification process.

For aforementioned reasons, a bi-level reduced surrogate model is proposed as a computationally inexpensive alternative to identify material parameter of the MMC fracture criterion in this paper. In the recent literature [29, 30], reduced surrogate model was initially used to parameterize numerical material representation based on proper orthogonal decomposition, extended to approximate the constitutive behavior of local material for a given microstructure in a topology optimization problem [31]. This method is robust and shows high accuracy in both of these numerical applications. Moreover, surrogate model [32–34] utilizes an approximation based on the results computed at various points in a design space to replace a complex one. The approximation obtained from the surrogate model does not represent the low fidelity versions of computational models derived by simplifying the physics of underlying phenomena. Instead, the surrogate-model based approximation aims to reconstruct the input-output relationship implemented by numerical simulations [35]. Particularly, the application of the surrogate model in this identification process significantly reduces the number of required fracture tests. In order to construct surrogate model properly, the Diffuse Approximation [29–31, 36–38] is widely used. And, its specialized properties highlight its effectiveness in a range of computational mechanics application varying from structural optimization to surface interpolation for identification of material parameters. A surrogate model based on the Diffuse Approximation is proposed in the current work to empirically capture the non-linear evolution of material parameters on the fracture onset under uniaxial loading condition. Consequently, the aim is to develop a computationally affordable but accurate model, which utilizes a small set of training data obtained from bi-level models: local critical elements and global 3D finite element (FE) fracture models, to identify the material parameters of

MMC criterion for a given DP steel. In the proposed method, the surrogate model is used as an approximation tool associated with the *successive* Design of Experiments (DOE) and *enhanced* design space transformation techniques [39–42], given current fracture onset displacement and fracture strain.

2. Experimental work

2.1. Material description

In this work, fracture testing specimens are extracted from 1.6 mm thickness cold rolled DP590 steel sheets. The loading axis of each specimen is always located along the rolling direction. Fig. 1 gives the micrograph of DP590 steel using Quanta FEG 250 scanning electron microscope (SEM), which shows an obvious ferritic/martensitic microstructure. OLYMPUS Stream software [43] is used to analyze the phase proportions of the material and it provides the martensite and ferrite as 22% and 78% respectively (see [6] for additional details of the material and its phase fraction information).

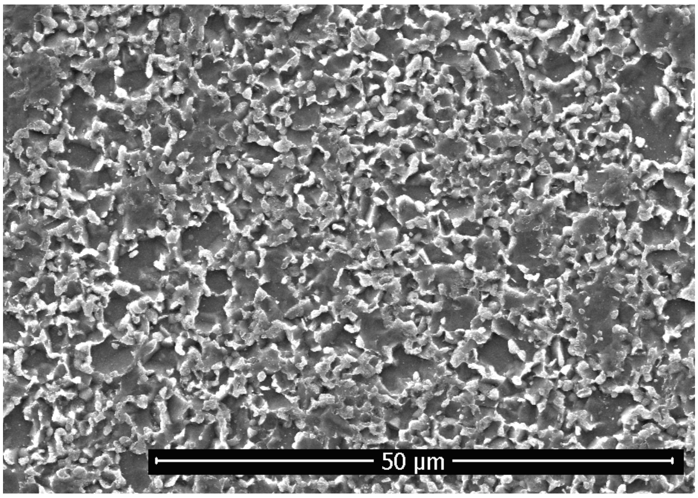

Figure 1: Topography image of the investigated DP590 steel.

2.2. Specimen and experimental procedure

Initial characterization of fracture criterion is performed using tensile tests on a smooth and two notched flat specimens with different notch radius of $R = 20$ mm and $R = 1$ mm, and the detailed geometries are given in Fig. 2. The smooth specimen has a 100 mm gauge length and a 10 mm gauge width. Similarly, the notched 20 mm and 1 mm specimens have the same gauge width of 10 mm and different gauge length of 40 mm and 20 mm, respectively. Experiments are carried out using Zwick Z020 tensile test machine at room temperature, with a quasi-static displacement rate of 2 mm/min. In these tests, the displacement was measured using an electronic extensometer. The experimental measurements are given in Fig. 3. For each specimen, a maximum force is reached before fracture.

The onset of fracture is defined by the sudden drop of load in the normalized load-displacement curves (i.e. the corresponding point indicated by a red cross mark at the end of each curve). And,

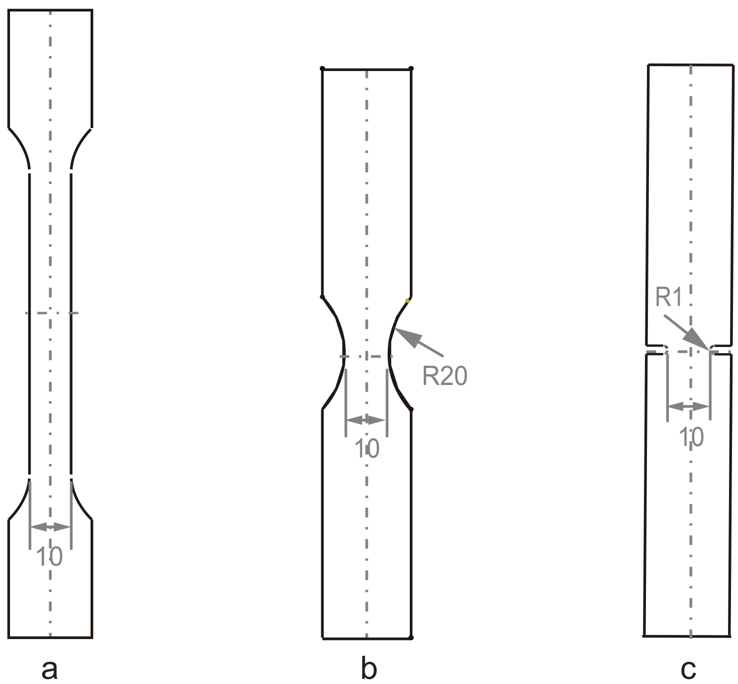

Figure 2: Geometry information of smooth and notched specimens.

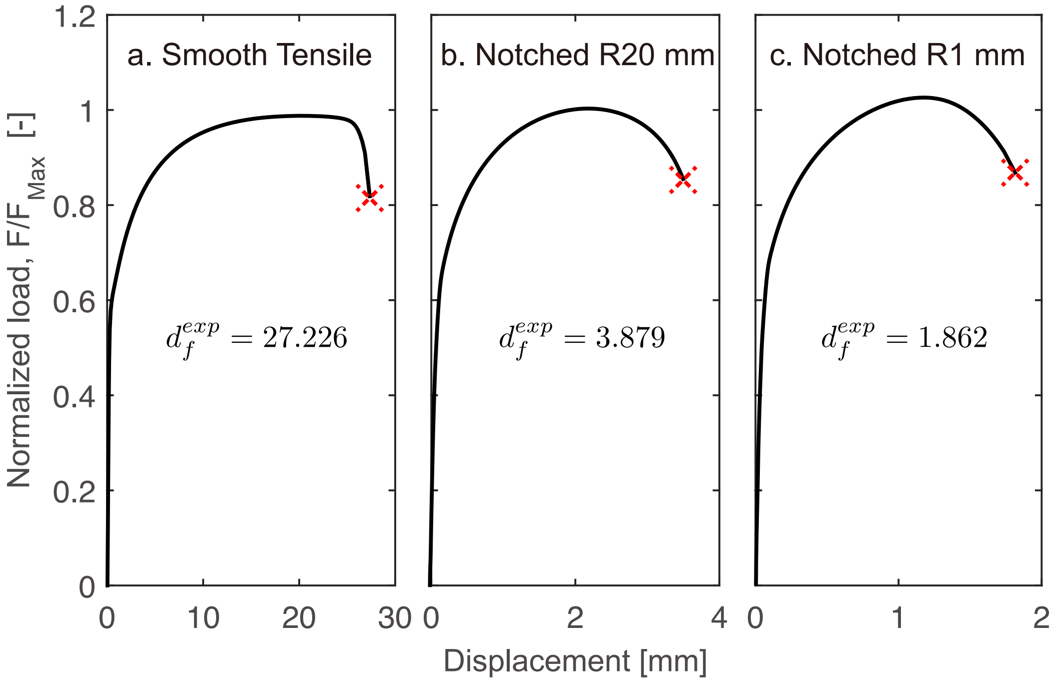

Figure 3: Measured load-displacement curves and average fracture onset displacements for (a) smooth, notched tensile specimens with (b) 20 mm and (c) 1mm open cutouts..

the corresponding relative displacement between the test region boundaries is referred as fracture onset displacement. Three specimens of each geometry are tested to ensure the reproducibility of the results. The variations in the measured fracture displacement are around 2.5% for smooth specimen, and less than 1.5% for each notched specimens. The average fracture onset displacement for each specimen is also given in Fig. 3. Moreover, the initial fracture strain (ε_f) is given by:

$$\varepsilon_f = \ln\left(\frac{A_0}{A_f}\right) \tag{1}$$

where A_0 and A_f are initial and fracture cross section areas of a specimen, respectively. Since the cross section after fracture is irregular, this initial fracture strain is considered only as an approximation. In order to approach the exact value, an iteration scheme is utilized. More detail of the scheme is given in Section 4.4.

3. Target material constitutive modeling

3.1. Plasticity model

The elasto-plastic behavior of DP590 steel is described by the J2 plasticity, in which a classical Swift power law [44] is utilized to describe the true stress-strain until the plastic localization occurrence:

$$\sigma = K(\varepsilon_0 + \varepsilon_p)^n \tag{2}$$

where σ is the true stress, and ε_p is the plastic strain. K, ε_0 and n are material constants to be fitted. Using the flow curve (Fig. 4) corresponding to the smooth specimen, the constants are identified as shown in Table 1.

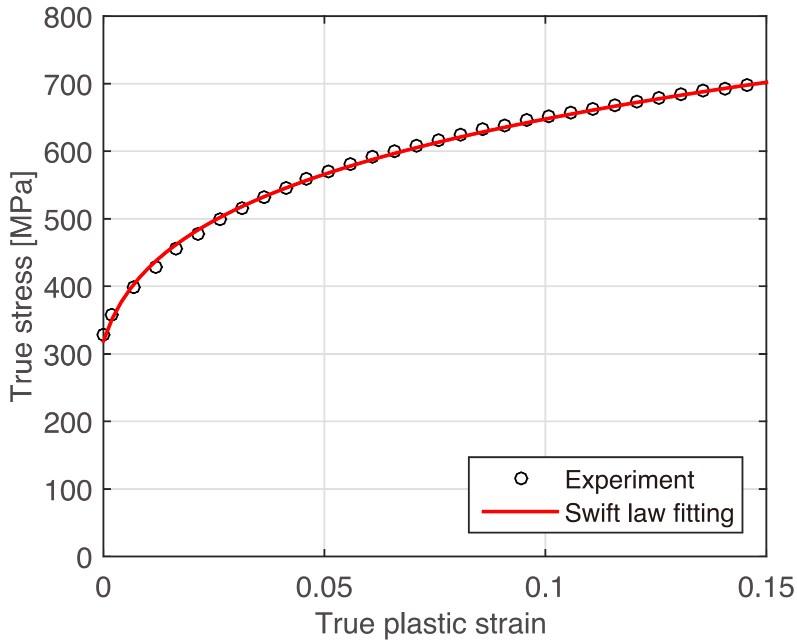

Figure 4: Measured and Swift law fitting flow curves of DP590 steel.

Table 1: Strain hardening parameters.

K (MPa)	ε_0	n
1080	0.0032	0.21

The red solid line in Fig. 4 represents the identified flow curve, and the circles indicate the measurements. Since no obvious discrepancy is found in the comparison, Swift law is utilized along with the von Mises yield criterion to simulate the plastic flow behavior of DP590 steel.

3.2. MMC fracture model

A modified version Mohr-Coulomb (MMC) criterion is identified as an adequate fracture model for the identification work. The original Mohr-Coulomb criterion [21] is written in stress space and assumes that the fracture occurs when the combined normal and shear stresses on any plane of normal vector **n** meet the following condition:

$$\max_{\mathbf{n}}(\tau + c_1\sigma_n) = c_2 \tag{3}$$

where c_1 is the coefficient of friction and c_2 is the shear resistance. Bai and Wierzbicki [19] transformed Eq. (3) into the space of stress triaxiality (η), normalized Lode angle parameter ($\bar{\theta}$) and equivalent plastic strain to fracture ($\bar{\varepsilon}_f$) assuming the proportional monotonic loading, in a spherical coordinate system. The resulted explicit expression for the fracture strain is given by:

$$\begin{aligned}\bar{\varepsilon}_f(\eta,\bar{\theta}) = &\left\{\frac{K}{c_2}\left[c_3 + (c_\theta - c_3)\frac{\sqrt{3}}{2-\sqrt{3}}\left(\sec\left(\frac{\pi}{6}\bar{\theta}\right) - 1\right)\right]\right.\\ &\left.\left[\sqrt{\frac{1+c_1^2}{3}}\cos\left(\frac{\pi}{6}\bar{\theta}\right) + c_1\left(\eta + \frac{1}{3}\sin\left(\frac{\pi}{6}\bar{\theta}\right)\right)\right]\right\}^{-\frac{1}{n}}\end{aligned} \tag{4}$$

and

$$c_\theta = \begin{cases} 1 & \text{for} \quad \bar{\theta} \geq 0 \\ c_4 & \text{for} \quad \bar{\theta} < 0 \end{cases} \tag{5}$$

where K and n are the fitting parameters obtained using the classical Swift law in Eq. (2). c_3 and c_θ describe the dependence of the underlying plasticity model on the third stress invariant. The free model parameters (c_1, c_2, c_3, c_4) have to be calibrated based on fracture experiments.

However, due to the application range and nature of the experimental testing condition (specimen geometry and loading condition), the normalized Lode angle parameter ($\bar{\theta}$) is always greater than 0. Based on Eq. (5), a simplified three parameter version of the modified Mohr-Coulomb fracture (MMC3) [23] model can be obtained by fixing the parameter c_θ as 1. Therefore, the remaining unknown parameters become (c_1, c_2, c_3).

In Eq. (4), the stress triaxiality is defined as the ratio between hydrostatic stress (σ_m) and von Mises equivalent stress ($\bar{\sigma}$):

$$\eta = \frac{\sigma_m}{\bar{\sigma}}, \quad \sigma_m = \frac{1}{3}tr(\boldsymbol{\sigma}) \tag{6}$$

with $-\infty \leq \eta \leq \infty$. The Lode angle parameter is normalized as:

$$\bar{\theta} = 1 - \frac{6\theta}{\pi}, \quad 0 \leq \theta \leq \frac{\pi}{3} \tag{7}$$

and lies in the range of $-1 \leq \bar{\theta} \leq 1$. The Lode angle is computed using:

$$\cos(3\theta) = \frac{27}{2} \frac{(\sigma_{\mathrm{I}} - \sigma_m)(\sigma_{\mathrm{II}} - \sigma_m)(\sigma_{\mathrm{III}} - \sigma_m)}{\bar{\sigma}^3} \tag{8}$$

where $\sigma_{\text{I-III}}$ are the principal stresses. Further details of space transformation can be found in the work of Bai and Wierzbicki [19].

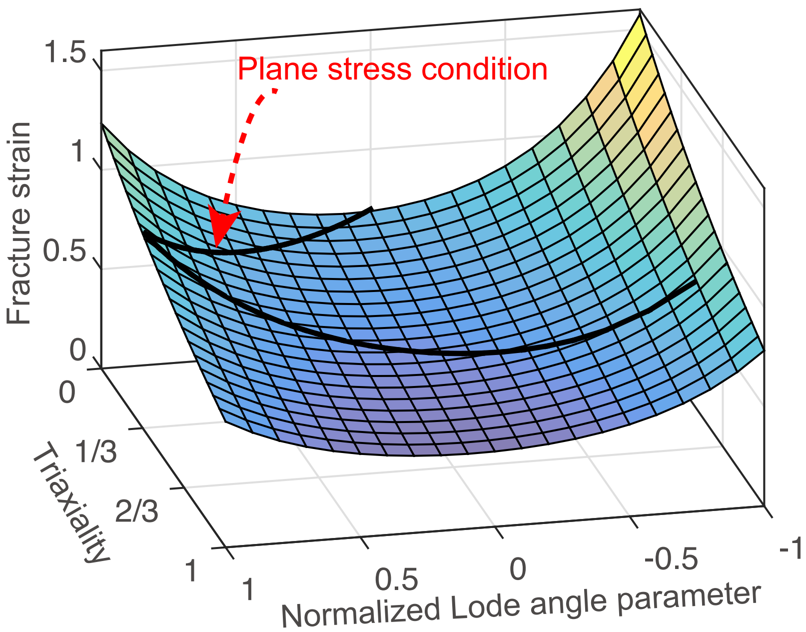

Figure 5: Illustration of the MMC fracture criterion in $(\eta, \bar{\theta}, \bar{\varepsilon}_f)$ space. The solid line depicts the plane stress condition.

In order to facilitate the utilization of the MMC model for sheet metals, Wierzbicki and Xue [17] proposed a plane stress condition, which relates the stress triaxiality and the normalized Lode angle parameter by:

$$\cos\left[\frac{\pi}{2}(1 - \bar{\theta})\right] = -\frac{27}{2}\eta\left(\eta^2 - \frac{1}{3}\right) \tag{9}$$

Therefore, a plane stress fracture curve (the solid line in Fig. 5) can be projected on the fracture surface (in Fig. 5) using Eq. (4). Fig. 6 depicts the fracture locus in the plane of $(\eta, \bar{\varepsilon}_f)$, which needs to be calibrated and determined based on the aforementioned fracture tests. The analytical stress states of the smooth and notched specimens are denoted with red, green and blue dots in Fig. 6.

In the case of proportional loading, the corresponding damage evolution indicator of the fracture prediction model can be expressed using an integration that is proposed by Bai and Wierzbicki [20]. The integral formulation is governed by a linear relationship between the damage indicator

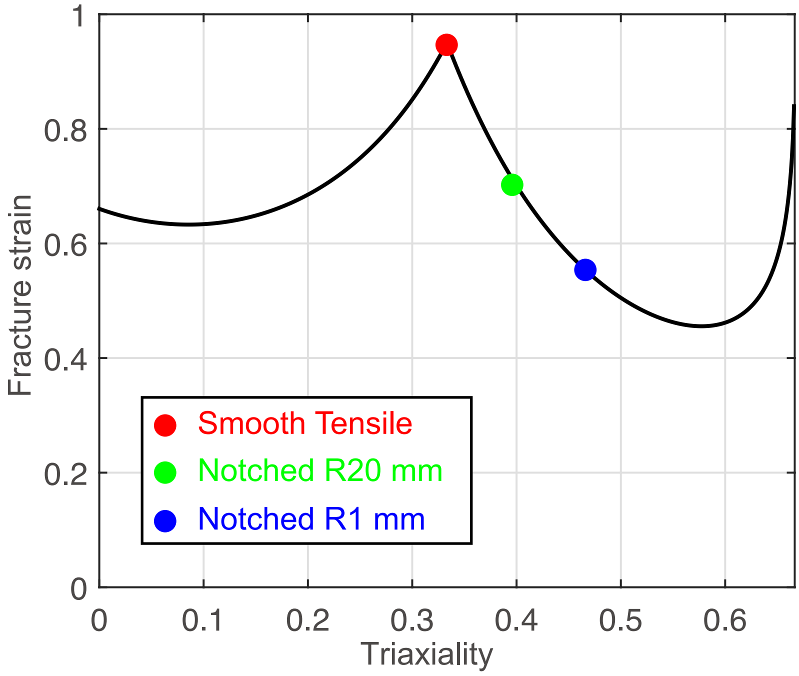

Figure 6: Projection of the MMC fracture surface in $(\eta, \bar{\varepsilon}_f)$ plane. Red, green and blue dots depict the smooth, notched 20 mm and 1 mm specimens, respectively.

and the equivalent plastic strain:

$$D(\bar{\varepsilon}_p) = \int_0^{\bar{\varepsilon}_p} \frac{d\bar{\varepsilon}_p}{\bar{\varepsilon}_f(\eta, \bar{\theta})} \tag{10}$$

When the limit of ductility is reached, the damage indicator $D(\bar{\varepsilon}_p)$ of the critical material element reaches the threshold value of 1, and leads to the elimination of the element from FE model. The instantaneous displacement corresponding to the critical element elimination, is referred as the predicted fracture onset displacement, while the exact value is obtained from experiments. Hence, the identification of the parameters of MMC fracture criterion is performed using an optimization approach to minimize the discrepancy between the predicted and measured results.

4. Identification process based on bi-level reduced surrogate model

As presented in Section 3.2, the original MMC criterion is simplified to a MMC3 criterion using Eq. (4) and (5). In order to identify those three unknown parameters (c_1, c_2, c_3), a bi-level reduced surrogate model is developed based on the combination of *successive* DOE and Diffuse Approximation approaches.

4.1. Bi-level modeling reduction strategy

This section focuses on the bi-level modeling reduction strategy used to construct the surrogate model.

In order to calibrate the MMC3 criterion, numerical simulations are initially performed on the three fracture specimens described in Section 2.2 combined with the strain hardening parameters

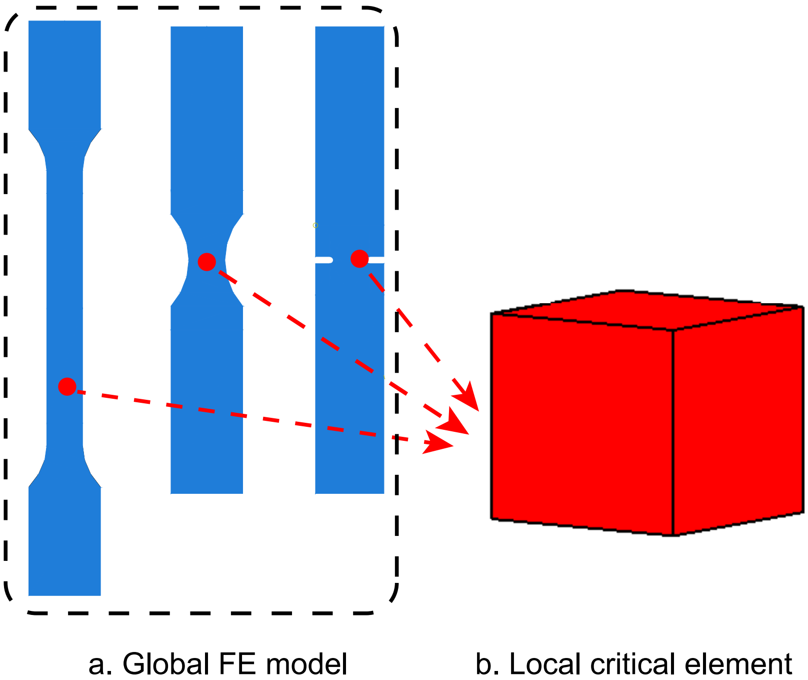

Figure 7: Illustration of the bi-level reduced strategy: (a) global FE model and (b) local critical element model.

given in Table 1. These preliminary simulations do not include fracture. All specimens are meshed with eight-node 3D solid, reduced integration elements (C3D8R in Abaqus/Explicit) [45]. After that, the MMC3 fracture model is programmed in Fortran code as a VUMAT file, which can be utilized to predict the fracture onset displacement of each specimen. When the critical element is removed from the specimen, the displacement is considered as the predicted fracture onset displacement. Although the specimen geometries are symmetrical about the transverse plane, the initiation of the fracture and resulted fracture surfaces do not always occur along the same symmetric plane. Therefore, whole specimens are considered in the global FE models to investigate the fracture behavior, as shown in Fig. 7a. Meanwhile, in order to reduce the computational time, a local critical element is selected according to the strain localization level and the fracture initiation normally occurs in this particular element during the simulation, as shown in Fig. 7b. Initially, prior to choose the local critical element in each specimen, a FE simulation without fracture criterion has been performed. According to the strain localization during the deformation process, the element with highest equivalent plastic strain value is selected. Moreover, in following computation with fracture criterion, the critical element number is verified in each iteration steep with the previous iteration step. If they do not remain the same, additional computation (reccording the stress state history of the new critical element) is performed within the current iteration step. From both predicted and experimental observations, it is identified that the local critical elements of the smooth and 20 mm notched tensile specimens are always located at the center of the longitudinal cross-section, while the third specimen reveals the critical elements along the edge of the open notch, as shown in Fig. 7. The main reason of this phenomenon indicates that stress concentration is caused by the geometric irregularity at the vicinity of the 1 mm radius notch.

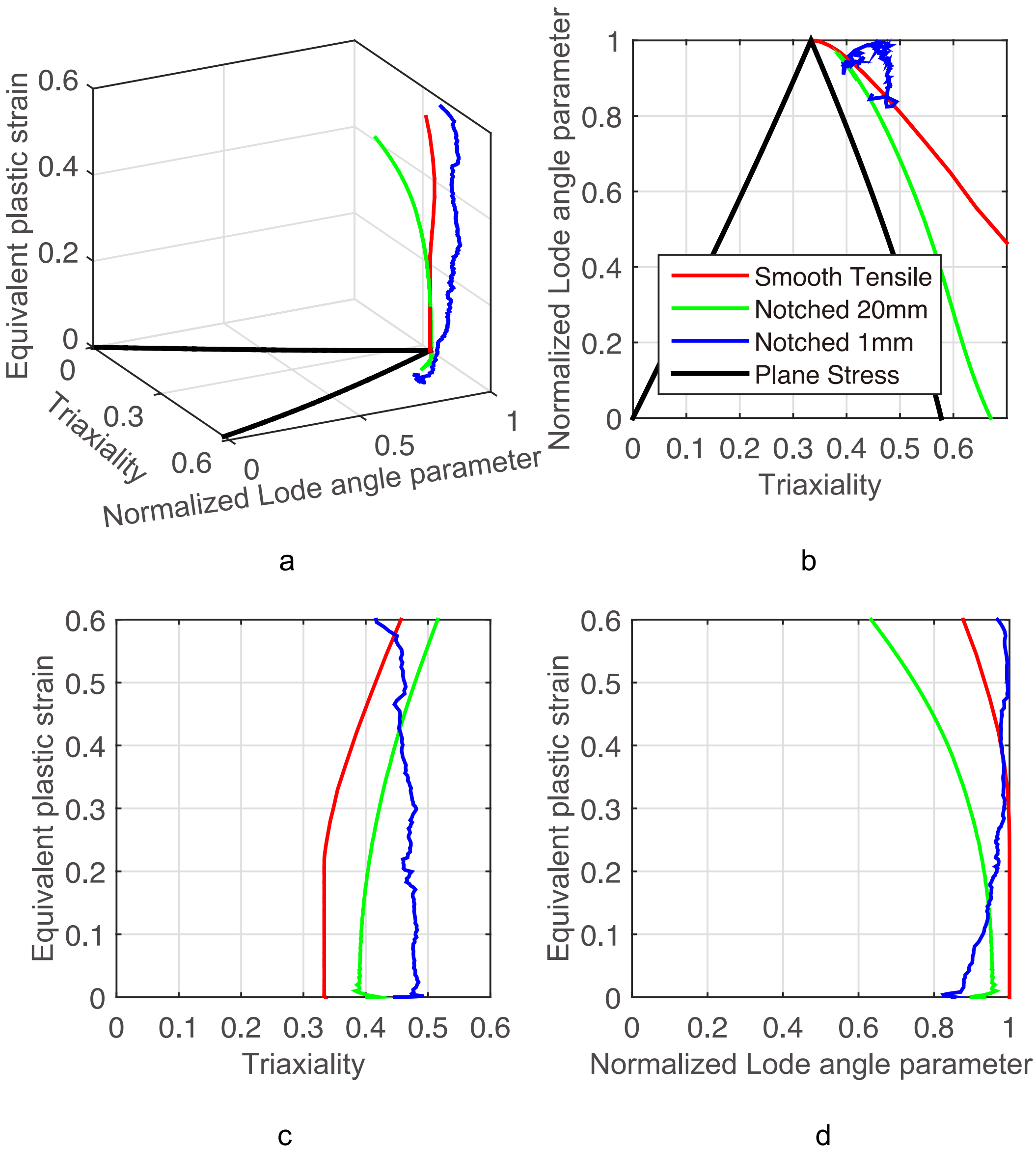

Figure 8: Plane stress condition and stress state histories of the local critical element obtained for each tensile specimen without fracture in: (a), $(\eta, \bar{\theta}, \bar{\varepsilon}_p)$ space, (b), $(\eta, \bar{\theta})$ plane, (c), $(\eta, \bar{\varepsilon}_p)$ plane and (d), $(\bar{\theta}, \bar{\varepsilon}_p)$ plane.

Additionally, the critical element is not at the center of the smooth tensile specimen. It is mainly because the strain localization firstly appears at this fracture position. And, in the initial simulation where no fracture model has been utilized, necking also takes place at the same position, not at the center of the specimen. Moreover, experimental observations also support the simulation result.

The histories of the stress triaxiality, normalized Lode angle parameter and equivalent plastic strain in the local element are recorded with time and plotted in Fig. 8. The values of η, $\bar{\theta}$ and $\bar{\varepsilon}_p$ are also projected on the different individual planes, as shown in Fig. 8b-d. Plane stress finite element model is not able to capture the damage and thus the finite element calculations are performed with 3D model. Moreover, there is no analytical solution exists for 3D case of this problem while existing analytical solution is based on plane stress condition. Therefore, in this figure, the stress state and equivalent plastic strain histories are compared with analytical ones under plane stress condition (the black line in Fig. 8a and b). It can be obviously found that the curves of smooth and 20 mm notched tensile specimens closely resemble with the analytical solutions obtained for the plane stress condition. However, in the case of 1 mm notched tensile specimen, those curves are significantly different from other two cases. This is mainly because, the corresponding local critical element is not located in the center of specimen's longitudinal cross-section, and the strain localization largely affects the curve in Fig. 8b (while strain is more diffuse for the other two specimens). That is, the location of the local critical element is highly sensitive to the strain localization for the 1 mm notched specimen. Moreover, as those specimens undergo necking, the stress states significantly deviates from the analytical solution.

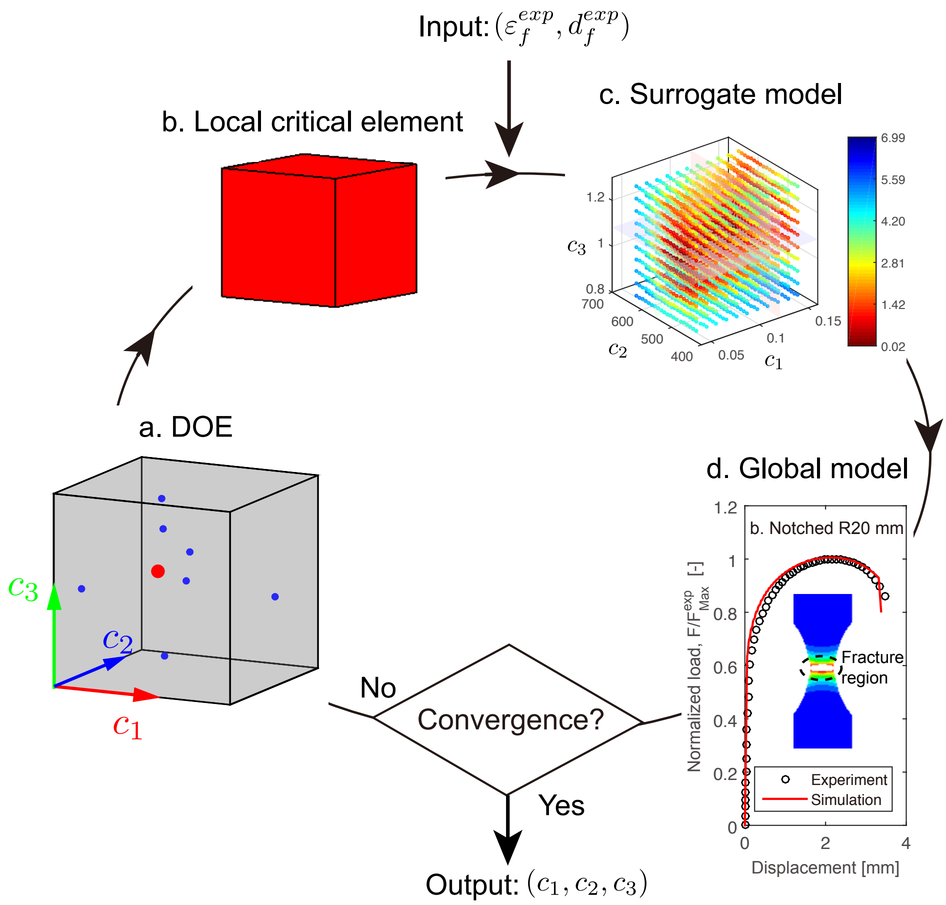

Figure 9: Flowchart of the Bi-level modeling reduction strategy.

Based on the paths of stress states, training experimental points of unknown parameters (c_1, c_2, c_3) in DOE can be calculated within the local critical element. The corresponding surrogate model is constructed according to Diffuse Approximation. Fig. 9 gives a schematic illustration of the bi-level modeling reduction strategy. In summary, the strategy consists of following steps:

1. Initial material parameters (c_1^0, c_2^0, c_3^0) are considered as the center (red dot in Fig. 9a) to create the DOE for the first iteration. Fracture strains of each training experimental points (blue dots in Fig. 9a) are calculated based on the stress states of the local critical elements (Fig. 9b) using Eq. (4);
2. Fracture strain prediction for the whole DOE space is computed using Diffuse Approximation. A surrogate model (Fig. 9c) of the least square error (*LSE.*) between the predicted and measured fracture strain is constructed to identify the material parameters. Identified material parameters of each iteration are determined from the surrogate model by:

$$\textbf{Argmin}\, LSE. = \frac{1}{m}\sum_{i=1}^{m}(\tilde{\varepsilon}_{fi}(\mathbf{c}) - \varepsilon_{fi}^{exp})^2 \tag{11}$$

   where $\tilde{\varepsilon}_{fi}(\mathbf{c})$ is the predicted fracture strain at the point $\mathbf{c}$, ε_{fi}^{exp} is the measured fracture strain, and m is the number of various specimen geometries;
3. The obtained parameters are then introduced within the global model (Fig. 9d) to compute the corresponding *LSE.* of the fracture onset displacement:

$$LSE. = \frac{1}{m}\sum_{i=1}^{m}(d_{fi} - d_{fi}^{exp})^2 \tag{12}$$

   where d_{fi} and d_{fi}^{exp} are predicted and measured fracture onset displacements, respectively. The DOE of next iteration is designed by shifting the center to the identified parameters and halving the DOE variation;
4. Converged material parameters are identified until the variation of DOE space and *LSE.* of the fracture onset displacement (in Eq. 12) reach sufficiently acceptable ranges.

The proposed bi-level modeling reduction strategy can guarantee not only the accuracy of identification process with a limited number of experimental tests, but also significantly reduce the computational time. Further details of the aforementioned approaches and methods are given in the following sections.

4.2. Fracture strain prediction using Diffuse Approximation

By following the procedure given in the flowchart (Fig. 9), a 3D material parameter DOE containing H points is designed in each iteration, expressed by matrix $\mathbf{C} = [\mathbf{c}_1, \mathbf{c}_2, \mathbf{c}_3] = [\mathbf{c}^1, \mathbf{c}^2, \mathbf{c}^3, \ldots, \mathbf{c}^K]^T$. Let $\boldsymbol{\varepsilon}_f(\mathbf{C})$ denotes the $K \times 3$-dimensional fracture strain computed based on the stress state histories in local critical elements. The surrogate model of the fracture strain prediction for the whole DOE space is constructed using the method of Diffuse Approximation [46]:

$$\tilde{\boldsymbol{\varepsilon}}_f(\mathbf{C}) = \mathbf{p}(\mathbf{C})^T \mathbf{a}(\mathbf{C}) \tag{13}$$

where $\mathbf{p} = [p_1, p_2, p_3, \ldots]^T$ is the polynomial basis vector. In 3D case, the polynomial basis vector can be expressed in terms of the material parameters for the MMC3 criterion:

$$\mathbf{p} = [1, c_1, c_2, c_3, \ldots]^T \tag{14}$$

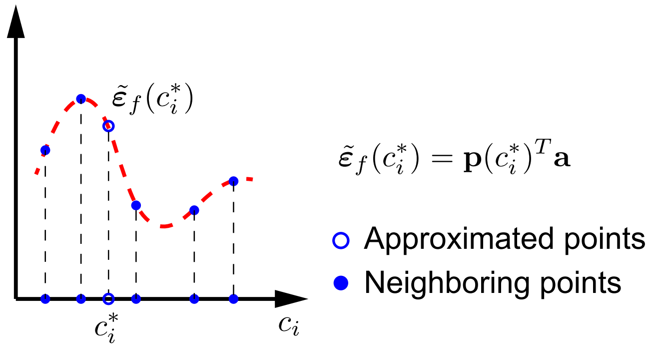

Figure 10: Illustration of the Diffuse Approximation procedure used to construct the surrogate model of fracture strain.

The vector of coefficients $\mathbf{a} = [a_1, a_2, a_3, \dots]^T$ is the minimizer of function defined by:

$$J(\mathbf{a}) = \frac{1}{2}\sum_{k=1}^{K} w(||\mathbf{c} - \mathbf{c}^k||)\Big(\mathbf{p}^T\mathbf{a} - \boldsymbol{\varepsilon}_f(\mathbf{c}^k)\Big)^2 \tag{15}$$

where $w(||\mathbf{c} - \mathbf{c}^k||)$ is the Gaussian weighting function depending on the Euclidean distance d between the approximated point $\mathbf{c}$ and the neighboring point $\mathbf{c}^k$:

$$w(||\mathbf{c} - \mathbf{c}^k||) = e^{-(\frac{d}{h})^2} \tag{16}$$

in which h is a fixed parameter reflecting the anticipated spacing between the neighboring points. It can be used to smooth the small fluctuation in the data [47].

Fig. 10 illustrates the approximation procedure, for a given fracture strain value of DOE training point. The corresponding approximated values for the whole design space are locally interpolated using Diffuse Approximation. Therefore, we construct the surrogate model including the *LSE*. between approximated and measured fracture strain for each specimen, given by Eq. (11). A set of optimal parameters are identified for each iteration by minimizing the objective function.

4.3. Design and transformation of DOE

In Section 4.2, a Diffuse Approximation approach is presented to construct the surrogate model. The surrogate model uses a set of points in the design space to determine an optimum approximation. Numerical experiments are performed in local critical elements for this set of points in the DOE. The method used to design and transform the DOE space is schematically depicted in Fig. 11.

As illustrated in Fig. 11, the main idea behind this method is to use an initial guess point (green dots in Fig. 11) within a sufficiently large design space at the beginning to select the experimental points (blue dots). It must guarantee that the first design space is big enough to contain the exact solution. After that, the identified points (red dot) determined using Eq. (11) is considered as the new center of design space (panning algorithm) with a smaller DOE variation (zooming algorithm) to reselect the experimental points. Further details of the panning and zooming algorithms are available in the literature [39]. But in this paper, the *nouvel* combination of these two DOE

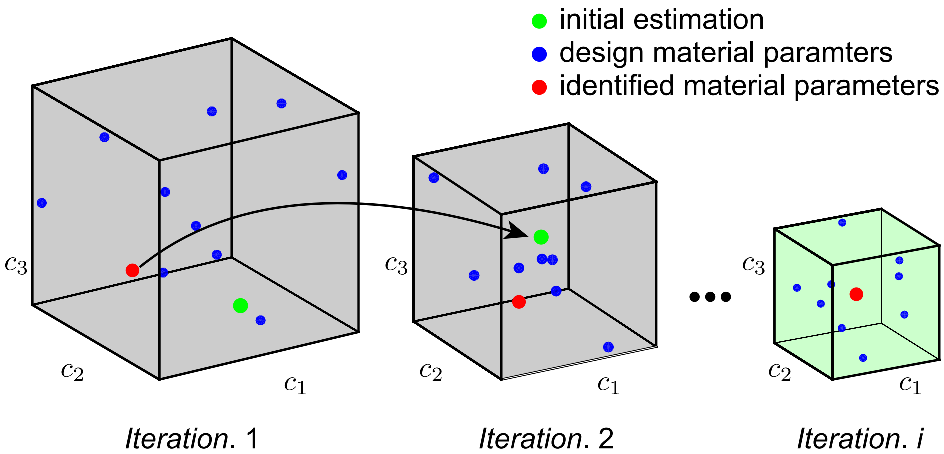

Figure 11: Illustration of the *successive* DOE design and transformation.

space algorithms, called as *panning & zooming algorithm*, has been utilized. Fig. 11 shows the schematic illustration of the *panning & zooming algorithm*. The whole DOE design and transformation process is repeated until convergence is reached. In the converged iteration, the center and identified points may be overlapped or located nearby.

4.4. Adaptive correlation between fracture onset displacement and strain

In our experimental test plan, since no digital image correlation (DIC) technique is used to capture the simultaneous strain when damage initially appears in those critical elements. The initial input fracture strain is computed using Eq. (1) based on experimental measurements, and it provides only an approximation of the fracture strain. Therefore, an iterative procedure including the fracture onset displacement is used to minimize the error between the exact and approximate fracture strain values. In each iteration step, an *adaptive deviation* of fracture onset displacement is firstly computed as:

$$\Delta d_{fi} = d_{fi} - d_{fi}^{exp} \tag{17}$$

Secondly, the new fracture strain is otained using the adaptive deviation:

$$(\varepsilon_{fi}^{exp})_{new} = (\varepsilon_{fi}^{exp})_{old} + \ln\left(1 + \frac{\Delta d_{fi}}{L_{0i}}\right) \tag{18}$$

where d_{fi} and d_{fi}^{exp} are the fracture onset displacements obtained from the global level simulation and experimental measurements, respectively. L_{0i} is the initial effective length in the test region of each specimen. This *adaptive correlation* is utilized to ensure that the fracture strain target varies around the exact value with a decreasing error that eventually becomes negligible.

5. Results and discussion

5.1. Mesh dependency of MMC3 fracture criterion

Generally, the MMC3 fracture criterion is a strain-based model; thus, the simulation result is dramatically affected by the mesh size. Essentially, high strain gradients are persistent in necking zones so that the calculated normalized load-displacement curves and fracture onset displacements are highly dependent on the mesh size. Therefore, before applying our proposed identification method, a mesh sensitivity study is preformed to determine an appropriate element size that can be utilized in this work. Fig. 12-14 illustrate the mesh size dependency of the normalized load-

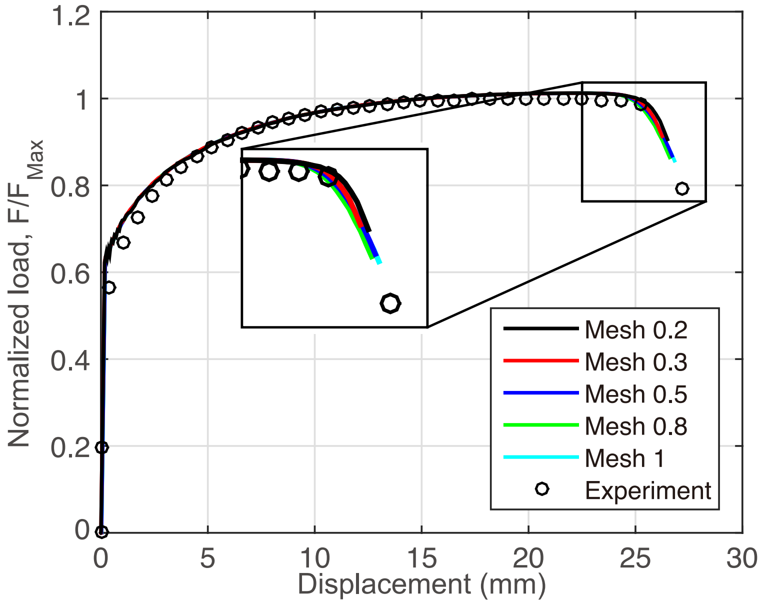

Figure 12: Predicted and experimental normalized load-displacement curves obtained the smooth tensile specimen.

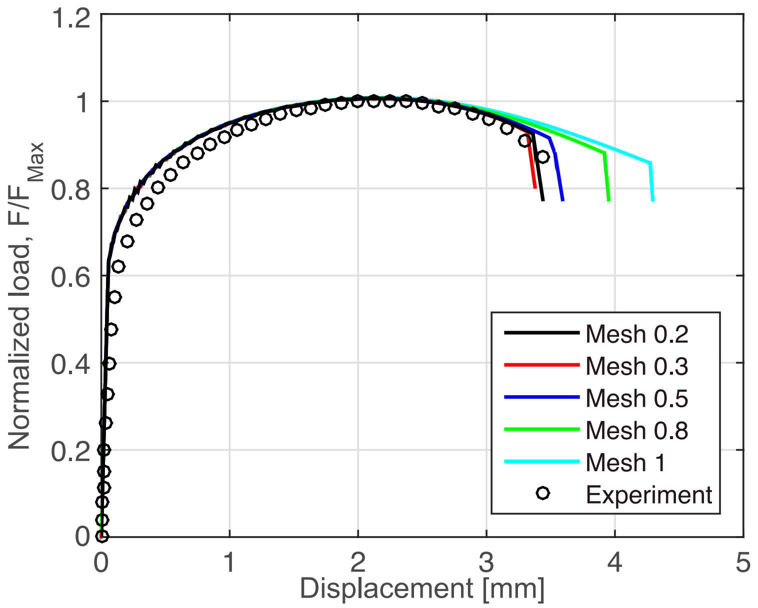

Figure 13: Predicted and experimental normalized load-displacement curves for the R20 mm notched tensile specimen.

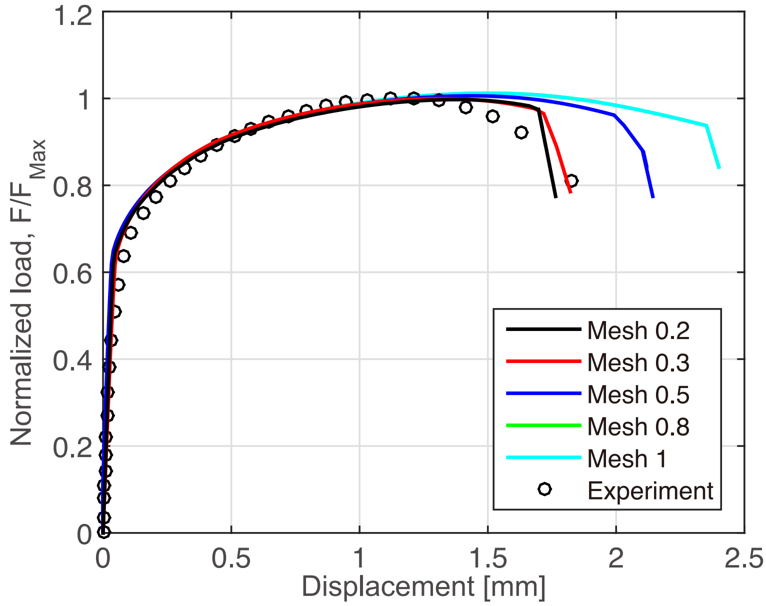

Figure 14: Predicted and experimental normalized load-displacement curves for the R1 mm notched tensile specimen.

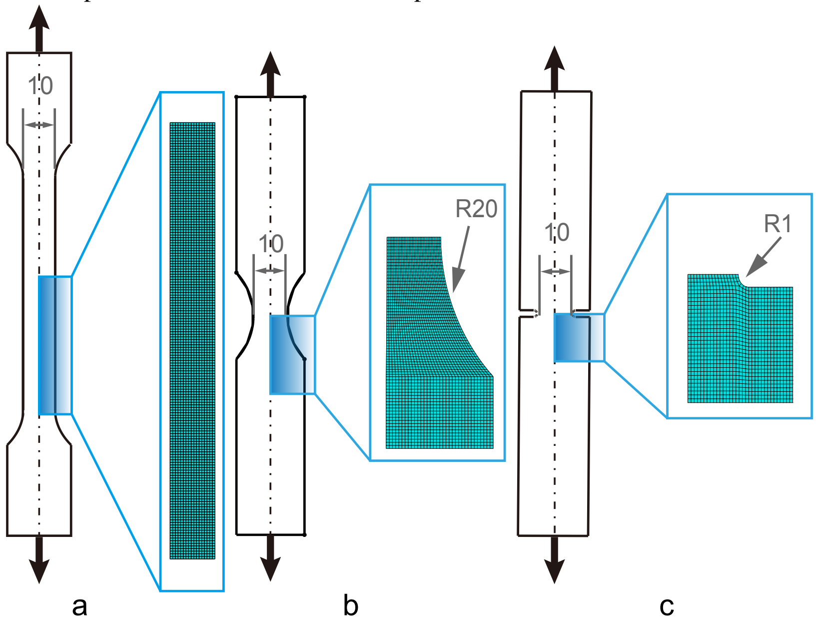

Figure 15: FE model with element length of 0.3 mm of: (a) smooth, (b) R20 mm and (c) R1 mm notched specimens.

displacement curves obtained for the smooth and notched tensile specimens, with element length varying from 0.2 mm to 1 mm. For the smooth tensile test, the difference resulted from the mesh size is not obvious. But, in other two cases, mesh size has a dramatic influence on the simulation results. Convergence is reached when element length comes to 0.3 mm (red solid lines) or less than 0.3 mm. In order to guarantee the accuracy of the calculation and reduce the computational cost, the converged element length of 0.3 mm is used in the identification process, as shown in Fig. 15.

5.2. *MMC3 fracture criterion characterization for DP590 steel*

The methodologies proposed in the previous sections are used to search the solution of the identification problem for the current fracture tests. A quadric polynomial basis (2nd-order), consisting of 10 terms, is adopted to construct the surrogate model in Eq. (11).

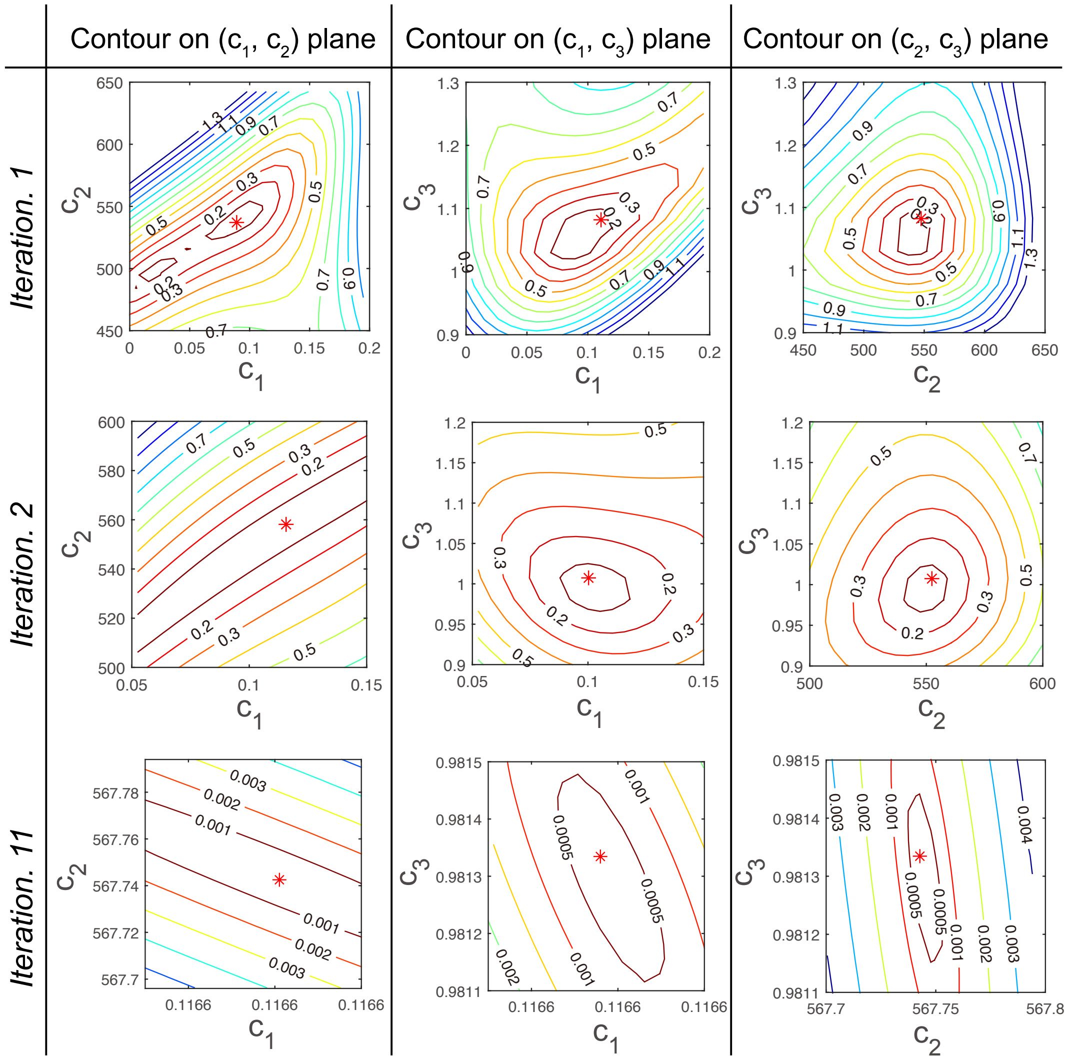

Figure 16: Projected contours of the *LSE*. obtained using the surrogate model between the measured and approximated fracture strains on various parameter planes.

In each iteration, 11 training experimental points are chosen from the DOE using Latin Hypercube Sampling (LHS) approach. The identified solution of each iteration is determined based on the fracture strain approximation for the whole DOE space. After that, the obtained material parameters are introduced to the global fracture test model. The *adaptive correlation* between the displacement and strain at the fracture onset, is computed to overcome the limitation of the current test plan. Hence, these three free parameters of MMC3 fracture criterion for DP590 steel are identified using the convergence condition given by:

$$\mathbf{Argmin}\, LSE. = \frac{1}{m}\sum_{i=1}^{m}(d_{fi} - d_{fi}^{exp})^2 \tag{19}$$

The error in the identification is given by the *LSE*. between the measured and predicted fracture onset strain and displacement for each tensile specimen.

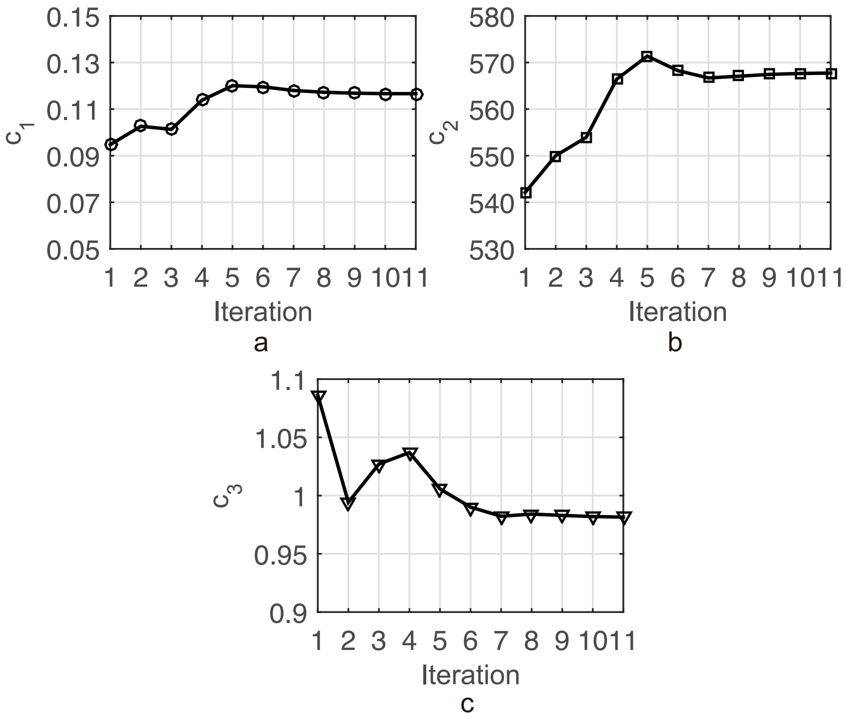

Figure 17: Convergence curves for the parametric identification of (a) c_1, (b) c_2 (unit: MPa) and (c) c_3.

Based on experience of numerical experiments, first identification process is begun with the initial material parameters of (0.1, 600 MPa, 1.03), lies within the reasonable ranges of the first DOE: $c_1 \in [0, 0.2]$, $c_2 \in [450, 650]$ (unit: MPa) and $c_3 \in [0.9, 1.3]$.

Successive design spaces and corresponding *LSE*. obtained from the surrogate model between the measured and approximated fracture strains of Iteration 1, 2 and 11 are shown in Fig. 16. Since the surrogate model is four-dimensional, projected contours on various parameter planes are given to illustrate its tendency. In each iteration, the optimal parameters are identified using Eq. (11). And, the red star in each design space represents these identified material parameters for the corresponding iteration. For example, the identified parameters are (0.094, 542.105 MPa, 1.086) and (0.103, 550 MPa, 0.994) in the first and second iteration, respectively. During the subsequent iterations, the DOE size reduces until the converged results are obtained. When it comes to Iteration 11, material parameters vary within a small range of 1×10^{-4} for c_1, 0.1 MPa for c_2, and 0.5×10^{-3} for c_3.

Fig. 17a, b and c show convergence curves for the parametric identification of c_1, c_2 and c_3,

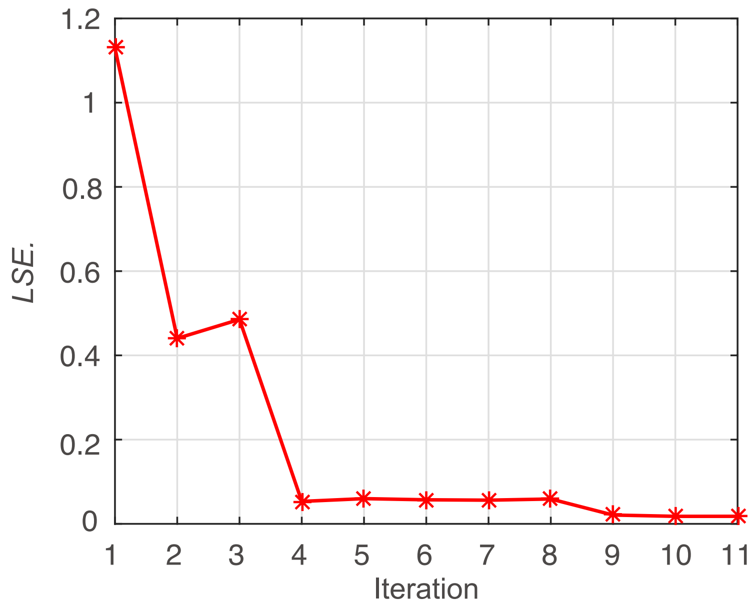

Figure 18: Progressive reduction of the *LSE.* between the measured and predicted fracture onset displacements with the identified material parameters for each iteration.

respectively. These results clearly indicate that after Iteration 7, each material parameter fluctuates around the converged value. Fig. 18 illustrates the progressive reduction of the *LSE.* between the measured and predicted fracture onset displacements with the identified material parameters from global FE simulation. Obvious decreases are found, and it stabilizes at around 0.02 after Iteration 9. Note that the *LSE.* is more reliable if the design space is smaller for each iteration. Hence, the result of Iteration 11 is more suitable than that of Iteration 9. Moreover, the final identified material parameters for MMC3 fracture criterion are reached as (0.117, 567.748 MPa, 0.982) in the first application.

5.3. Validation of the robustness

5.3.1. Second application case: identification with a different initial guess

Our first application to identify the material parameters of MMC3 fracture criterion for DP590 steel, exhibits that the bi-level reduced surrogate model has the capability. In order to validate the robustness of the proposed method, a second application with a different initial guess of material parameters (0.05, 550 MPa, 1.1), are adopted to begin the iterative computation. In this paper, we also aim to minimize the *LSE.* between the measured and predicted fracture onset displacements. The same range of design space in the first application are used.

In addition, the corresponding results are depicted in Fig. 19 and 20. In this case, the fluctuation of each parameter stabilizes after 6 iterations. During Iteration 7, the *LSE.* has already reduced to 0.02. Therefore, the final material parameters are identified from 9th iteration, as (0.117, 567.039 MPa, 0.978). These results indicate concur with the first application case, while the discrepancy is negligible. The negligible discrepancy is still arisen from the proposed DOE and its transformation algorithms, that can be reduced by increasing the number of iterations. This comparison clearly

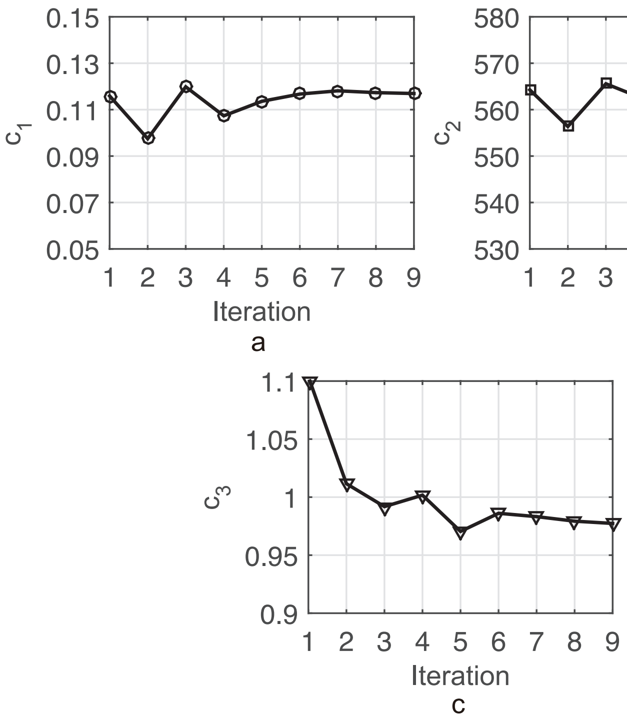

Figure 19: Convergence curves for the parametric identification of (a) c_1, (b) c_2 (unit: MPa) and (c) c_3, with second group of initial parameter values.

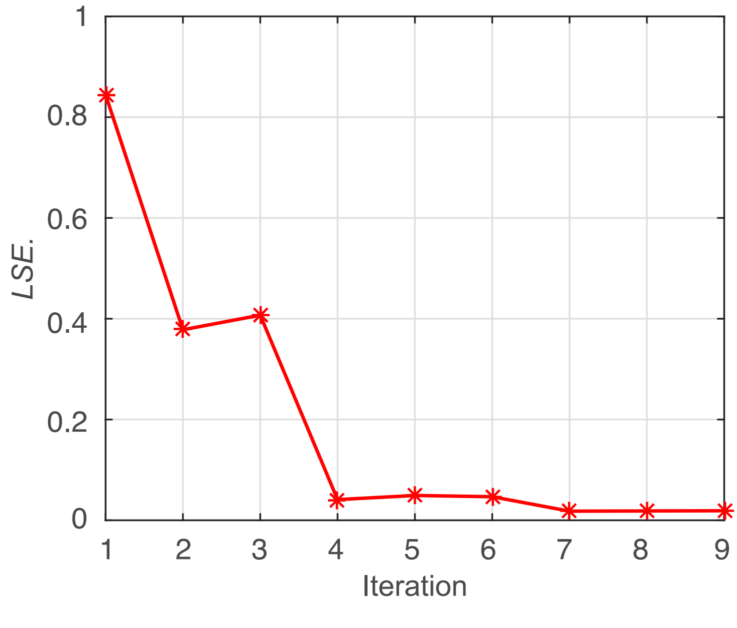

Figure 20: Progressive reduction of the *LSE.* between the measured and predicted fracture onset displacements with identified material parameters for the second application.

shows that the identification is independent of the initial guess; thus, it confirms the robustness of the identification process for this MMC3 fracture criterion.

5.3.2. *Validation of the identification method*

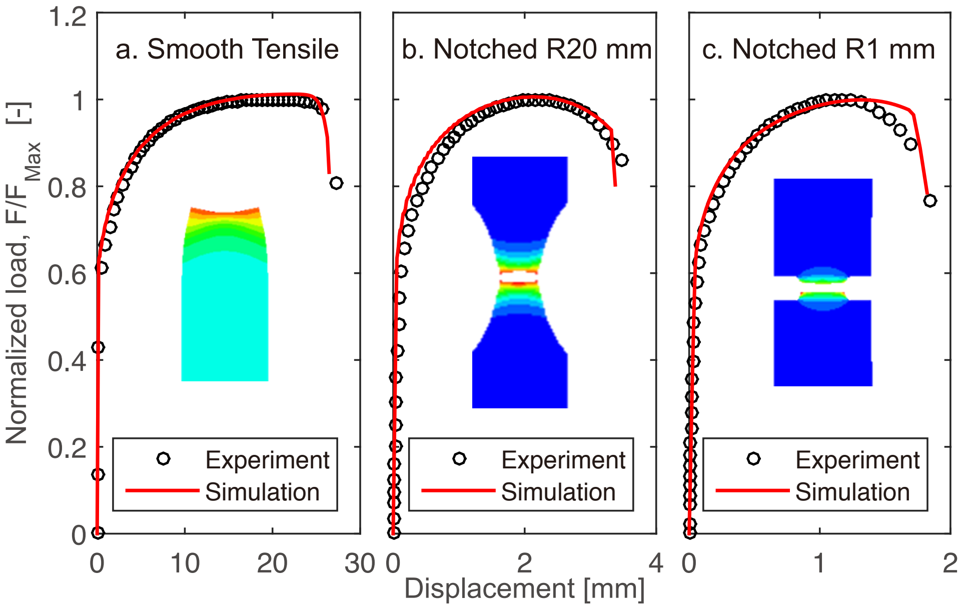

Figure 21: Comparison between predicted and measured load-displacement curves for (a) smooth and notched tensile specimens with (b) 20 mm and (c) 1 mm open cutouts.

For the purpose of validation, comparisons of the normalized load-displacement curves acquired from the experimental measurements and simulations with identified material parameters are depicted in Fig. 21. A good agreement is achieved between the measured and predicted results. Especially, the predicted fracture onset displacements closely resemble with the experimental measurement. It indicates the accuracy and reliability of the identified material parameters using the proposed bi-level reduced surrogate model. Additionally, the fracture location of each tensile specimen, which is also shown in Fig. 21, corroborates the experimental observation. It also supports the effectiveness of our proposed method.

The fracture locus of the MMC3 fracture criterion with identified material parameters is plotted in Fig. 22. The MMC3 fracture model shows a complex dependency on the stress triaxiality. For low stress triaxialities ($0 < \eta < 1/3$), the fracture strain reveals as U-shape function of triaxiality. While for the intermediate triaxialities ($1/3 < \eta < 2/3$), the fracture strain firstly decreases with triaxiality, and then it changes its path to rise rapidly.

6. Conclusions

The ductile fracture has been investigated extensively over decades. Numerous efforts have been made to calibrate the ductile fracture models with massive quantity of experimental tests. In this paper, a bi-level reduced surrogate model, which requires quite a limited number of tests, has been proposed to identify the material parameter of the MMC3 fracture criterion. The proposed method combines Diffuse Approximation and *successive* Design of Experiments (DOE) approaches to construct the surrogate model.

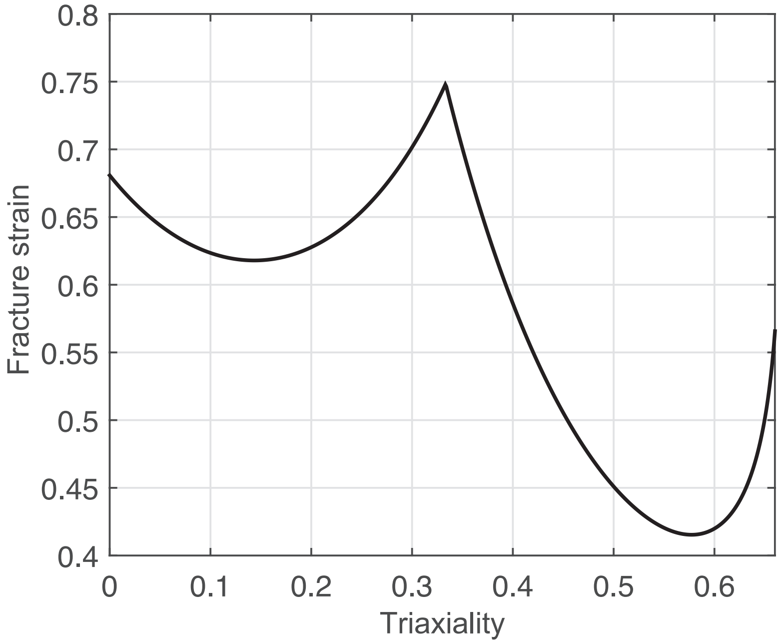

Figure 22: Fracture locus of the MMC3 fracture criterion with identified material parameters: $c_1 = 0.117$, $c_2 = 567.748$ MPa and $c_3 = 0.982$.

The bi-level reduced surrogate model is successfully implemented to build local critical element and global fracture tensile test models in each iteration. At the local level, Latin Hypercube Sampling algorithm is adopted to select a finite number of training points, in which the corresponding fracture strains are computed. Diffuse Approximation is utilized to construct the surrogate model of fracture strain that ensures the accuracy as well as reduces the computational cost. By minimizing the *LSE*. between the approximated and measured fracture strains, identified parameters are determined and introduced in the global model. At the global level, the relevant fracture onset displacements are obtained using fracture tensile test simulations. Consequently, an *adaptive correlation term* between fracture onset strain and displacement is computed to update the target fracture strain in the following iteration steps. Meanwhile, the new design space of material parameters is redesigned to reduce its size and center with the identified values, using the *panning & zooming algorithm*. The proposed identification method helps to simplify the characterization of the ductile fracture criterion.

Our protocol was validated for DP590 steel with the use of numerical simulations and experimental measurements. During the first trial of the proposed model, the converged solution is achieved at 11th iteration, while the second trial only required 9 iteration steps. Results obtained from these two trials show a close agreement, and it indicates the robustness of this method to identify the material parameters. Further investigation on the robustness and reliability of the proposed method has been confirmed with different initial guess. Moreover, the predicted load-displacement curves using the identified material parameters concurs the measured results. This study provides a novel numerical technique to identify the material parameters of ductile fracture criterion based on a surrogate model. This method could be implemented for various ductile materials and further extended with strain-rate and/or temperature dependent material identification problems.

Acknowledgements

The authors thank Mr. Liang Meng from Laboratoire Roberval, Université de Technologie de Compiègne, for the valuable discussions on the design and transformation of DOE and Diffuse Approximation method. This work was funded by ESI Group and China Scholarship Council (CSC).

References

[1] N. Kim, G. Thomas, Effects of morphology on the mechanical behavior of a dual phase Fe/2Si/0.1C steel, Metallurgical Transactions A 12 (3) (1981) 483–489.

[2] M. Sarwar, R. Priestner, Influence of ferrite-martensite microstructural morphology on tensile properties of dual-phase steel, Journal of Materials Science 31 (8) (1996) 2091–2095.

[3] U. Liedl, S. Traint, E. Werner, An unexpected feature of the stress–strain diagram of dual-phase steel, Computational Materials Science 25 (1) (2002) 122–128.

[4] W. Bleck, S. Papaefthymiou, A. Frehn, Microstructure and tensile properties in dual phase and trip steels, Steel Research International 75 (11) (2004) 704–710.

[5] R. H. Wagoner, G. R. Smith, Advanced high strength steel workshop, Arlington, Virginia, USA (2006) 1–122.

[6] Y. Hou, T. Sapanathan, A. Dumon, P. Culière, M. Rachik, A novel artificial dual-phase microstructure generator based on topology optimization, Computational Materials Science 123 (2016) 188–200.

[7] V. Uthaisangsuk, Modelling of damage and failure in multiphase high strength dp and trip steels, Engineering Fracture Mechanics 78 (3) (2011) 469–486.

[8] A. Ramazani, Y. Li, K. Mukherjee, U. Prahl, W. Bleck, A. Abdurakhmanov, M. Schleser, U. Reisgen, Microstructure evolution simulation in hot rolled DP600 steel during gas metal arc welding, Computational Materials Science 68 (2013) 107–116.

[9] M. Eshraghi, M. A. Tschopp, M. A. Zaeem, S. D. Felicelli, Effect of resistance spot welding parameters on weld pool properties in a DP600 dual-phase steel: a parametric study using thermomechanically-coupled finite element analysis, Materials & Design 56 (2014) 387–397.

[10] P. J. Zhao, Z. H. Chen, C. F. Dong, Failure analysis based on microvoids damage model for dp600 steel on in-situ tensile tests, Engineering Fracture Mechanics 154 (2016) 152–168.

[11] F. A. McClintock, A criterion for ductile fracture by the growth of holes, Journal of Applied Mechanics 35 (2) (1968) 363–371.

[12] J. R. Rice, D. M. Tracey, On the ductile enlargement of voids in triaxial stress fields, Journal of the Mechanics and Physics of Solids 17 (3) (1969) 201–217.

[13] A. L. Gurson, Continuum theory of ductile rupture by void nucleation and growth: Part I: Yield criteria and flow rules for porous ductile media, Journal of Engineering Materials and Technology 99 (1) (1977) 2–15.

[14] P. Woelke, G. Z. Voyiadjis, P. Perzyna, Elasto-plastic finite element analysis of shells with damage due to microvoids, International journal for numerical methods in engineering 68 (3) (2006) 338–380.

[15] C. Reina, B. Li, K. Weinberg, M. Ortiz, A micromechanical model of distributed damage due to void growth in general materials and under general deformation histories, International Journal for Numerical Methods in Engineering 93 (6) (2013) 575–611.

[16] G. R. Johnson, W. H. Cook, A constitutive model and data for metals subjected to large strains, high strain rates and high temperatures, in: Proceedings of the 7th International Symposium on Ballistics, Vol. 21, The Hague, The Netherlands, 1983, pp. 541–547.

[17] T. Wierzbicki, L. Xue, On the effect of the third invariant of the stress deviator on ductile fracture, Impact and Crashworthiness Laboratory, Technical Report (136).

[18] Y. Bao, T. Wierzbicki, A comparative study on various ductile crack formation criteria, Journal of Engineering Materials and Technology 126 (3) (2004) 314–324.

[19] Y. Bai, T. Wierzbicki, A new model of metal plasticity and fracture with pressure and Lode dependence, International Journal of Plasticity 24 (6) (2008) 1071–1096.

[20] Y. Bai, T. Wierzbicki, Application of extended Mohr–Coulomb criterion to ductile fracture, International Journal of Fracture 161 (1) (2010) 1–20.

[21] O. Mohr, Welche umstände bedingen die elastizitätsgrenze und den bruch eines materials, Zeitschrift des Vereins Deutscher Ingenieure 46 (1524-1530) (1900) 1572–1577.

[22] M. Dunand, D. Mohr, Hybrid experimental–numerical analysis of basic ductile fracture experiments for sheet metals, International Journal of Solids and Structures 47 (9) (2010) 1130–1143.

[23] M. Dunand, D. Mohr, On the predictive capabilities of the shear modified Gurson and the modified Mohr–Coulomb fracture models over a wide range of stress triaxialities and Lode angles, Journal of the Mechanics and Physics of Solids 59 (7) (2011) 1374–1394.

[24] G. Gruben, O. Hopperstad, T. Børvik, Evaluation of uncoupled ductile fracture criteria for the dual-phase steel Docol 600DL, International Journal of Mechanical Sciences 62 (1) (2012) 133–146.

[25] F. Ebnoether, D. Mohr, Predicting ductile fracture of low carbon steel sheets: Stress-based versus mixed stress/strain-based Mohr–Coulomb model, International Journal of Solids and Structures 50 (7) (2013) 1055–1066.

[26] T. Eller, L. Greve, M. Andres, M. Medricky, A. Hatscher, V. Meinders, A. Van den Boogaard, Plasticity and fracture modeling of quench-hardenable boron steel with tailored properties, Journal of Materials Processing Technology 214 (6) (2014) 1211–1227.

[27] J. Papasidero, V. Doquet, D. Mohr, Ductile fracture of aluminum 2024-T351 under proportional and non-proportional multi-axial loading: Bao–Wierzbicki results revisited, International Journal of Solids and Structures 69 (2015) 459–474.

[28] M. Algarni, Y. Bai, Y. Choi, A study of inconel 718 dependency on stress triaxiality and lode angle in plastic deformation and ductile fracture, Engineering Fracture Mechanics 147 (2015) 140–157.

[29] L. Xia, B. Raghavan, P. Breitkopf, W. Zhang, Numerical material representation using proper orthogonal decomposition and diffuse approximation, Applied Mathematics and Computation 224 (2013) 450–462.

[30] L. Xia, B. Raghavan, P. Breitkopf, Towards surrogate modeling of material microstructures through the processing variables, Applied Mathematics and Computation 294 (2017) 157–168.

[31] L. Xia, P. Breitkopf, A reduced multiscale model for nonlinear structural topology optimization, Computer Methods in Applied Mechanics and Engineering 280 (2014) 117–134.

[32] W. Roux, N. Stander, R. T. Haftka, Response surface approximations for structural optimization, International Journal for Numerical Methods in Engineering 42 (3) (1998) 517–534.

[33] N. Slander, The successive response surface method applied to sheet-metal forming, in: First MIT Conference on Computational Fluid and Solid Mechanics, 2001, pp. 481–485.

[34] D. Wirtz, N. Karajan, B. Haasdonk, Surrogate modeling of multiscale models using kernel methods, International Journal for Numerical Methods in Engineering 101 (1) (2015) 1–28.

[35] P. Breitkopf, H. Naceur, A. Rassineux, P. Villon, Moving least squares response surface approximation: formulation and metal forming applications, Computers & Structures 83 (17) (2005) 1411–1428.

[36] P. Lancaster, K. Salkauskas, Surfaces generated by moving least squares methods, Mathematics of Computation 37 (155) (1981) 141–158.

[37] B. Nayroles, G. Touzot, P. Villon, Generalizing the finite element method: diffuse approximation and diffuse elements, Computational Mechanics 10 (5) (1992) 307–318.

[38] L. Xia, P. Breitkopf, Multiscale structural topology optimization with an approximate constitutive model for local material microstructure, Computer Methods in Applied Mechanics and Engineering 286 (2015) 147–167.

[39] L. Meng, P. Breitkopf, B. Raghavan, G. Mauvoisin, O. Bartier, X. Hernot, Identification of material properties using indentation test and shape manifold learning approach, Computer Methods in Applied Mechanics and Engineering 297 (2015) 239–257.

[40] L. Meng, P. Breitkopf, G. Le Quilliec, B. Raghavan, P. Villon, Nonlinear shape-manifold learning approach: Concepts, tools and applications, Archives of Computational Methods in Engineering (2016) 1–21.

[41] L. Meng, P. Breitkopf, G. Le Quilliec, An insight into the identifiability of material properties by instrumented indentation test using manifold approach based on ph curve and imprint shape, International Journal of Solids

and Structures.
[42] M. Liang, B. Raghavan, O. Bartier, X. Hernot, G. Mauvoisin, P. Breitkopf, An objective meta-modeling approach for indentation-based material characterization, Mechanics of Materials 107 (2017) 31–44.
[43] OLYMPUS Stream: User's Manual, Vol. 1, Olympus Soft Imaging Solutions GmbH, 2013.
[44] H. Swift, Plastic instability under plane stress, Journal of the Mechanics and Physics of Solids 1 (1) (1952) 1–18.
[45] ABAQUS/Explicit: User's Manual, Vol. 1, Hibbitt, Karlsson and Sorenson Incorporated, 2001.
[46] P. Breitkopf, A. Rassineux, P. Villon, An introduction to moving least squares meshfree methods, Revue Européenne des Éléments 11 (7-8) (2002) 825–867.
[47] M. Alexa, J. Behr, D. Cohen-Or, S. Fleishman, D. Levin, C. T. Silva, Computing and rendering point set surfaces, Visualization and Computer Graphics, IEEE Transactions on 9 (1) (2003) 3–15.